Photoacoustics 33 (2023) 100561

Contents lists available at ScienceDirect

Photoacoustics

journal homepage: www.elsevier.com/locate/pacs

# A frequency-domain model-based reconstruction method for transcranial photoacoustic imaging: A 2D numerical investigation

Hyungjoo Park [a], Junjie Yao [b], Yun Jing [a,*]

[a] The Graduate Program in Acoustics, The Pennsylvania State University, University Park, PA 16802, USA
[b] Department of Biomedical Engineering, Duke University, Durham, NC 27708, USA

ARTICLE INFO

*Keywords:*
Model-based method
Photoacoustic Imaging
Transcranial ultrasound

ABSTRACT

Phase aberration caused by the skull is a major barrier to achieving high quality photoacoustic images of human and non-human primates' brains. To address this issue, time-reversal methods have been used but they are computationally demanding and slow due to relying on solving the full-wave equation. The proposed approach is based on model-based image reconstruction in the frequency-domain to achieve near real-time image reconstruction. The relationship between an imaging region and transducer array elements can be mathematically described as a model matrix and the image reconstruction can be performed by pseudo-inverse of the model matrix. The model matrix is numerically calculated due to the lack of analytical solutions for transcranial ultrasound. However, this calculation only needs to be performed once for a given experimental setup and the same acoustic medium, and is an offline process not affecting the actual image reconstruction time. This non-iterative mode-based method demonstrates a substantial improvement in image reconstruction time, being approximately 18 times faster than the time-reversal method, all while maintaining comparable image quality.

## 1. Introduction

The brain, one of the most complex organs in our body, is still an unknown territory, and understanding its mechanisms is crucial to gain fundamental knowledge about human behavior, development, aging, disorder, or diseases [1,2]. While a wide range of different imaging modalities have been developed to visualize the structure of the nervous system and changes in brain functions, a comprehensive understanding of the brain requires a single map integrating in vivo brain functions at different spatiotemporal scales [3]. However, most current imaging modalities are limited in their ability to image the brain of human and non-human primates at different length scales, which hinders the creation of comprehensive brain maps. Therefore, recent studies on brain functions have dominantly utilized decoupled approaches. Two-photon microscopy has been used to image the brain of small animals at a microscopic scale, but it is not suitable for imaging the human brain due to its limited penetration depth [4,5]. On the contrary, functional magnetic resonance imaging (fMRI) can image the whole human brain at a macroscopic scale, but suffers from a poor spatiotemporal resolution [6,7]. Therefore, addressing this gap is crucial to achieve a better understanding of brain structures and functions.

Photoacoustic tomography (PAT) is a hybrid imaging modality that can embrace both microscopic and macroscopic realms with a consistent contrast mechanism and has the potential to fill the above-mentioned gap [8,9]. When a region of interest (ROI) is illuminated by a short laser pulse, the scattered light is absorbed by biomolecules such as oxyhemoglobin, deoxyhemoglobin, lipid, melanin, etc. The absorbed optical energy is then converted into heat which increases the temperature, resulting in thermal expansions. These thermoelastic expansions induce ultrasound waves and are subsequently detected by ultrasound transducer outside the ROI to form a photoacoustic image that maps the optical absorption of the biological tissue [10]. Since acoustic waves scattering is orders of magnitude weaker than that of optical waves in tissue, PAT provides higher resolution with greater penetration depth than optical imaging. Unlike conventional ultrasound imaging where the contrast depends on the acoustical properties of the tissue, PAT leverages contrast pertaining to the optical absorption of biomolecules, and therefore is better suited to examine brain functions including blood oxygenation and neurovascular coupling. Furthermore, PAT is free from ionizing radiation, and therefore it can be used on patients who require frequent monitoring of brain functions.

Although PAT can be used for both microscopic and macroscopic

* Corresponding author
*E-mail address:* yqj5201@psu.edu (Y. Jing).

https://doi.org/10.1016/j.pacs.2023.100561
Received 28 July 2023; Received in revised form 19 September 2023; Accepted 20 September 2023
Available online 21 September 2023

scale brain imaging to provide information about brain vasculature, oxygenation, brain responses to physiological and pathological challenges, and the metabolism of oxygen and glucose [11], this imaging modality still has some hurdles to overcome, and a major challenge is the phase aberration from the skull. Transcranial PAT has been used to probe the structure and hemodynamic responses of small animals [12,13] and human infants due to the availability of acoustic windows [14,15]. However, adult humans or non-human primates have relative thick skulls that can severely distort the photoacoustic (PA) signals and cause significant image reconstruction artifacts [16–18]. Therefore, it is important to develop an image reconstruction algorithm to compensate for the skull-induced distortion.

Recently, the time-reversal (TR) method has been actively studied in PAT due to its ability to correct distorted PA signals in heterogeneous media and provide accurate images by incorporating information about the medium heterogeneities (e.g., from CT scans [16]). However, the TR method necessitates full-wave simulations of wave propagation from the receivers to the ROI. This process can be time-consuming and may impede real or near real-time functional imaging of the brain [16,19–21]. Although the TR method can be employed as a post-processing tool to mitigate image artifacts, real-time functional imaging offers many essential advantages that are particularly significant in applications such as guiding neural stimulation and brain-computer interfaces (BCI), where online neuro-feedback is of utmost importance.

On the other hand, model-based (MB) methods have also been extensively studied because of their potential to achieve high quality images and fast image reconstruction [22–26]. From the PA forward model, PA signals can be represented as a linear combination of the initial pressure distribution $p_0$ and time derivative of Green's functions, and a model matrix (MM) can be formulated using this relation to establish a link between the PA signals and $p_0$. By employing inversion schemes, $p_0$ can be extrapolated from the acquired PA signals [27].

While delay-and-sum (DAS) [28] and back-projection (BP) [29] methods are computationally less demanding than MB methods, MB methods can provide high-quality images by accounting for sensor properties such as the element shape [26,30]. Furthermore, it has a more powerful quantification capacity that can be utilized for functional imaging. Provided that the experimental configuration remains identical, meaning the same medium and the transducer array, the MM calculation only needs to be performed once prior to imaging. Thereby, MB methods enable fast image reconstruction compared to TR method. However, most of the MB methods are only applicable to either homogeneous or weakly heterogeneous media [22–25,31,32]. For highly scattering media, iterative MB methods have been applied [33], but it remains a question whether non-iterative MB methods can be extended to highly scattering media such as the skull.

The main contribution of this work is the introduction of the first non-iterative MB method for real-time transcranial PAT. Prior to imaging, the MM is numerically calculated in the time-domain, which is then transformed to the frequency domain by employing the fast Fourier transform (FFT). To estimate the original initial pressure distribution for image reconstruction from the radio-frequency (RF) data received by the transducer array, pseudo-inversion of the MM is implemented. Although the calculation of the MM is still computationally intensive, it can be performed offline prior to imaging and only needs to be computed once for the same experimental configuration enabling repeated use for real-time or near real-time functional imaging. The performance of the FDMB method is evaluated through analysis of analytical RF data obtained from a 2D homogeneous medium, followed by numerical RF data obtained from a 2D heterogeneous medium using a rhesus monkey skull. To create realistic conditions, numerical RF data calculations take into account factors such as acoustic absorption, sensor frequency response, Gaussian noise, sensor location errors, and shear waves. The results indicate that the proposed FDMB method enables PAT image reconstruction through a rhesus monkey skull with similar image quality to the traditional TR method while achieving considerably faster reconstruction time.

The structure of this paper is as follows: Section 2 presents the theory of the FDMB method including the MM, pseudo-inversion, and data reduction. In Section 3, the performance of the FDMB method for homogeneous and heterogeneous media is assessed. Section 4 presents a discussion and conclusion of this work.

## 2. Methods

### 2.1. Photoacoustic forward problem

The acoustic pressure $p(\mathbf{x},t)$ in the forward photoacoustic model can be described by the following linear wave equation in the absence of absorption [34]:

$$\rho(\mathbf{x})\nabla\cdot\left(\frac{1}{\rho(\mathbf{x})}\nabla p(\mathbf{x},t)\right)-\frac{1}{c^2(\mathbf{x})}\frac{\partial^2 p(\mathbf{x},t)}{\partial t^2}=\frac{\Gamma}{c^2(\mathbf{x})}\quad\frac{\partial\mathscr{H}}{\partial t} \tag{1}$$

where $c$ is the speed of sound, and $\rho$ is the density, and both of which are functions of space. $\Gamma$ is the Grüneisen parameter indicating light absorbing efficiency which is defined as $\Gamma=\frac{c^2\beta}{C_p}$, where $\beta$ is the thermal coefficient of volume expansion and $C_p$ is the specific heat in constant pressure. When a short-pulsed laser excitation is within a stress confinement [35], the heating function can be separated as $\mathscr{H}=H_{\mathbf{x}}(\mathbf{x})\delta(t)$ where $H_{\mathbf{x}}(\mathbf{x})$ is the heat deposited in the fluid per unit volume. The solution of Eq. (1) can be shown to be (please refer to the appendix):

$$p(\mathbf{x},t)=\int\frac{p_0(\mathbf{x}')}{c(\mathbf{x}')^2}\frac{dG(\mathbf{x},t:\mathbf{x}',t')}{dt}\mathrm{d}\mathbf{x}' \tag{2}$$

where $p_0(\mathbf{x}')$ is the initial pressure ($t=0$) at location $\mathbf{x}'$, and $\frac{dG}{dt}$ is the time derivative of the Green's function which constitutes the time domain MM. When the medium is homogeneous, $c(\mathbf{x}')=c_0$. Eq. (2) can be discretized and rewritten in a summation form, which can be further transformed into the frequency domain by applying the Fourier transform (FT) as shown below:

$$\sum_{\mathrm{j}=1}^{N_s}\widehat{p}\left(\mathbf{x}_\mathbf{j},\omega\right)=\sum_{\mathrm{j}=1}^{N_s}\sum_{\mathrm{i}=1}^{N_p}j\omega\quad\frac{p_0\left(\mathbf{x}_\mathrm{i}'\right)}{c\left(\mathbf{x}_\mathrm{i}'\right)^2}\widehat{G}_\omega\left(\mathbf{x}_\mathrm{j},\mathbf{x}_\mathrm{i}'\right) \tag{3}$$

Let $p_0\left(\mathbf{x}_\mathrm{i}'\right)$ be the initial pressure distribution where $1\le \mathrm{i}\le N_p$ and $N_p$ being the total number of pixels to represent the ROI. Let $\widehat{p}\left(\mathbf{x}_\mathrm{j},\omega\right)$ be the PA signal received by the sensor where $1\le \mathrm{j}\le N_s$ and $N_s$ being the total number of the sensors. Assuming $\widehat{G}_{\mathrm{ij}}$ is the frequency-domain Green's function between pixel i and sensor j, Eq. (3) can be written using a single matrix operation:

$$\boldsymbol{P}(\omega)=\boldsymbol{M}(\omega)\cdot\boldsymbol{P_0} \tag{4}$$

where $\boldsymbol{P}(\omega)=[\widehat{p}(\mathbf{x}_1,\omega);\widehat{p}(\mathbf{x}_2,\omega);\cdots;\widehat{p}(\mathbf{x}_N,\omega)]$ is the vector for the sensors at frequency $\omega$, $\boldsymbol{P_0}=[p_0\left(\mathbf{x}_1'\right);p_0\left(\mathbf{x}_2'\right);\cdots;p_0(\mathbf{x}_{N_p}')]$ is the vector for the initial pressure distribution. $\boldsymbol{M}(\omega)=\frac{j\omega}{c^2}\cdot\left\{\widehat{G}_{\mathrm{ij}}\right\}_{1\le \mathrm{i}\le N_p,1\le \mathrm{j}\le N_s}$ is the frequency-domain MM which represents the core of the discretized forward model describing the relation between $\widehat{p}\left(\mathbf{x}_\mathrm{j},\omega\right)$ and $p_0\left(\mathbf{x}_\mathrm{i}'\right)$.

### 2.2. Inverse problem

The photoacoustic forward model can be used to calculate the PA signals at sensor locations using the linear equation described by Eq. (4). For the inverse problem where we are given $\boldsymbol{P}(\omega)$, $\boldsymbol{P_0}$ can be obtained using a method based on the least square error (LSQR) [36]:

$$P_{0,\mathrm{sol}}=\mathrm{argmin}\|M\cdot P_0-P\|_2^2 \tag{5}$$

where $\boldsymbol{P_{0,\mathrm{sol}}}$ is an approximated initial pressure distribution and $\|\cdot\|_2$

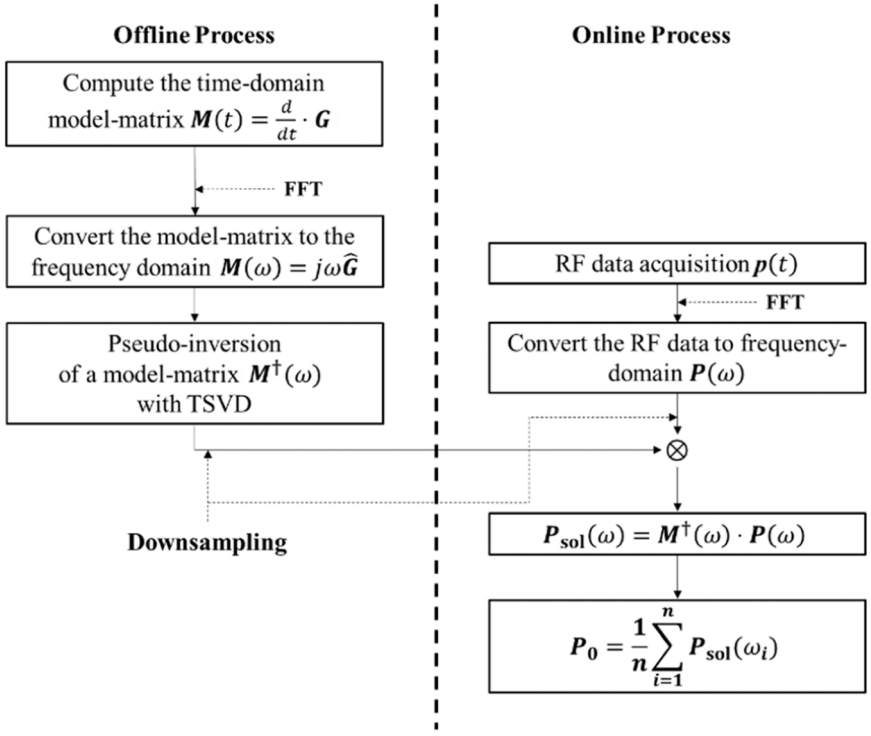


**Fig. 1.** Workflow of the frequency-domain model-based image reconstruction.

refers to $l_2$ norm. Another option is the Moore-Penrose pseudo inverse [37]:

$$P_0 = M^{\dagger}(\omega) \cdot P(\omega) \tag{6}$$

where $\boldsymbol{M}^{\dagger}(\omega) = \left(\boldsymbol{M}^{\boldsymbol{T}}\boldsymbol{M}\right)^{-1}\boldsymbol{M}^{\boldsymbol{T}}$ is the pseudo-inverse, and $T$ denotes the conjugate transpose operator. Normally, directly implementing Eq. (6) returns inaccurate solutions due to noise and limited data. Regularization can be employed to address this problem. A commonly used regularization scheme is the Tikhonov regularization [38,39], which yields the penalized least-square problem:

$$P_{0,\mathrm{sol}} = \mathrm{argmin}\|M \cdot P_0 - P\|_2^2 + \lambda\|P_0\|_2^2 \tag{7}$$

where $\lambda$ is the regularization parameter. Eq. (7) can be expressed as:

$$P_{0,\mathrm{sol}} = \left(M^T M + \lambda I\right)^{-1} M^T P \tag{8}$$

Several methods such as L-curve [40] and generalized cross validation (GCV) [38] methods can be used to determine the optimized $\lambda$. Another common regularization scheme to stabilize the inversion is the truncated singular value decomposition (TSVD) [37,41]. In this case, $\boldsymbol{M}$ can be decomposed as:

$$M = USV^T \tag{9}$$

where $\boldsymbol{U} = [u_1, u_2, \ldots, u_m] \in \mathbb{R}^{m \times m}$ and $\boldsymbol{V} = [v_1, v_2, \ldots, v_m] \in \mathbb{R}^{n \times n}$ are orthogonal matrices, and $\boldsymbol{S} = \mathrm{diag}[\sigma_1, \sigma_2, \ldots, \sigma_n] \in \mathbb{R}^{m \times n}$ is a diagonal matrix containing singular values $\sigma_n$ which are ordered so that $\sigma_1 \geq \sigma_2 \geq \cdots \geq \sigma_n \geq 0$. Regularization by the TSVD can be implemented by replacing singular values smaller than the threshold $\sigma_k$ to zeroes. Then, the pseudo-inverse of $\boldsymbol{M}$ based on the singular value decomposition (SVD) is:

$$M^{\dagger} = VS^{\dagger}U^T \tag{10}$$

where $\boldsymbol{S}^{\dagger} = \mathrm{diag}\left[\sigma_1^{-1}, \sigma_2^{-1}, \ldots, \sigma_k^{-1}\right], k \leq n$, and $k$ is the total number of non-zero singular values. Moore-Penrose pseudo inverse with the TSVD is used throughout this study.

### 2.3. Image reconstruction

Fig. 1 illustrates the workflow of the proposed algorithm. For heterogeneous media where analytical solutions are not available, full-wave simulations are first performed using the k-Wave MATLAB toolbox [42] to calculate the MM in the time domain. The calculated MM is then converted into the frequency domain by employing FFT. It should be noted that the frequency domain MM can be also computed directly by using a frequency-domain wave solver, without using FFT. Next, the pseudo-inverse of the MM is performed and the TSVD is selected as the regularization strategy. As the numbers of imaging pixels and transducer elements increase, the memory requirements for building the MM can become substantial, making it challenging to perform fast image reconstruction. To tackle this problem, down-sampling in the frequency domain is applied and frequency components above a threshold frequency are removed (truncation). Since most of the high frequency components are attenuated significantly when the PA signals pass through the skull layer due to its high absorption, it is possible to truncate the frequency components above a certain threshold. For this study, a down-sampling factor of 4 is selected and frequency components above 2 MHz are eliminated, unless otherwise specified. This offline process is performed prior to imaging and only requires to be conducted once for a given experimental setup and medium. Therefore, this process does not affect the actual image reconstruction time.

For the online process, the acquired RF data is transformed into the frequency domain via FFT. Since the MM is truncated and down-sampled, the RF data should also be truncated and down-sampled to match the frequency components before multiplication of the inversed MM and RF data ($\boldsymbol{P}_{\mathbf{sol}} = \boldsymbol{M}^{\dagger} \cdot \boldsymbol{P}(\boldsymbol{\omega})$). By applying the inverse fast Fourier transform (IFFT) to $\boldsymbol{P}_{\mathbf{sol}}$, the time-domain PA signals from the ROI is recovered and the initial pressure distribution $\boldsymbol{P_0}$ can be obtained at $t = 0$. However, since the RF data and the MM are truncated and down-sampled in the frequency domain, IFFT cannot be directly employed. Therefore, the following strategy is adopted to recover $\boldsymbol{P_0}$. The inverse discrete Fourier transform can be expressed as follows:

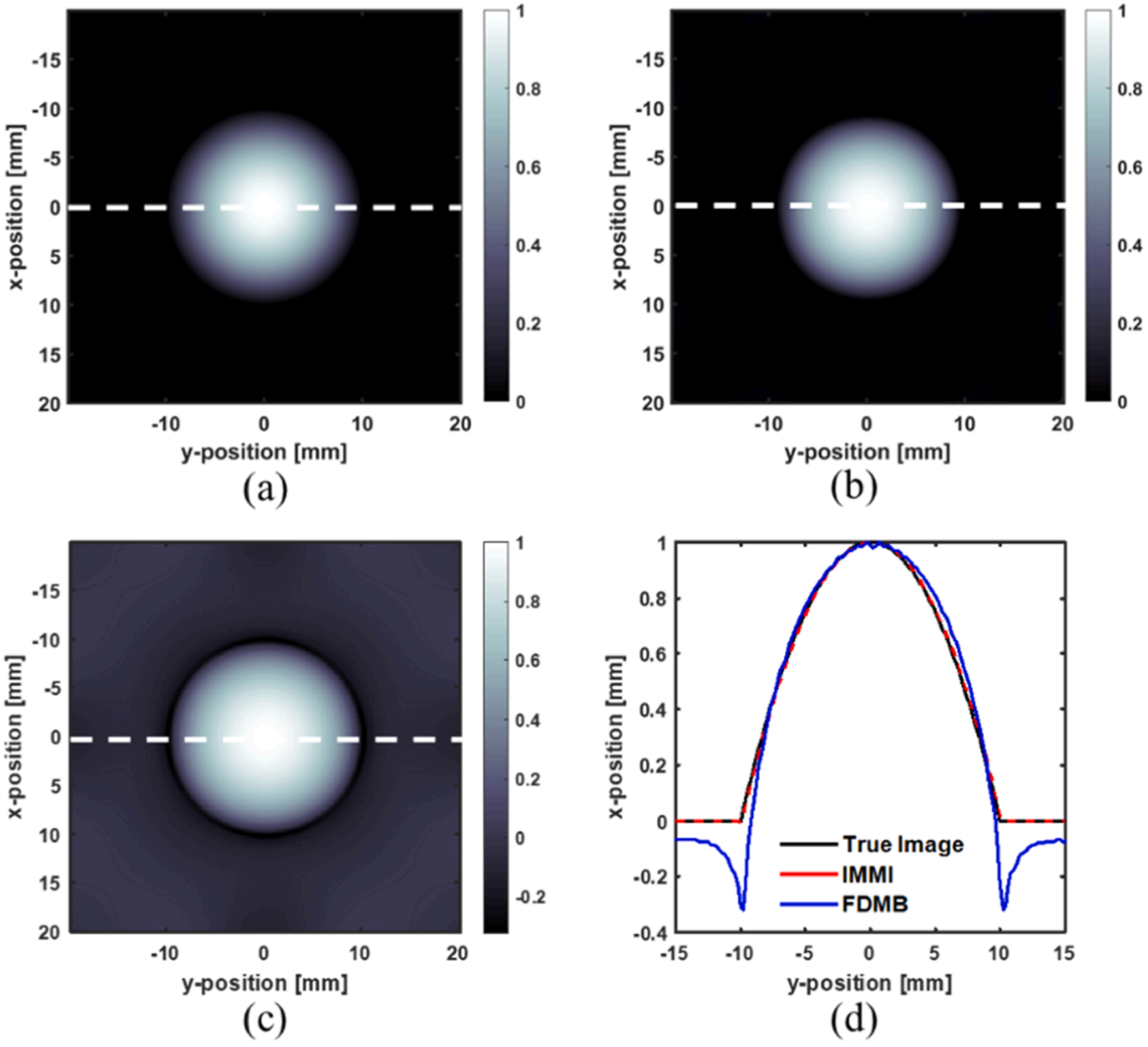


**Fig. 2.** (a) Initial pressure distribution of a paraboloidal source. Image reconstruction by (b) the IMMI method and (c) the FDMB method with the analytically calculated MMs. (d) Comparison between the true image, images obtained by the IMMI and the FDMB on a line crossing the center of the paraboloid source, as indicated by the white dashed lines in (a).

$$x(n) = \frac{1}{N}\sum_{k=0}^{N-1} X(k) e^{j\left(\frac{2\pi n}{N}\right)k} \tag{11}$$

where $x(n)$ is the sampled time series, $N$ is the total number of samples, and $X(k)$ is the sampled frequency signal. To recover $\boldsymbol{P_0}$, only $x(0)$ is needed where $n = 0$. Eq. (11) is then simplified to Eq. (12):

$$x(0) = \frac{1}{N}\sum_{k=0}^{N-1} X(k) \tag{12}$$

which is the summation of frequency components. The advantage of using Eq. (12) is that the truncated and down-sampled frequency data can be used to recover $\boldsymbol{P_0}$ and it is faster for processing large data compared to directly using the IFFT, which will enable us to achieve faster image reconstruction.

### 2.4. Model matrix and RF data generation

Numerical studies are conducted to verify the proposed FDMB method in 2D. The k-Wave MATLAB toolbox is used to generate the MM and numerical synthetic RF data, except for the homogeneous medium case, where analytical solutions are available. The speed of sound (SOS) and density of a rhesus monkey skull are extracted from a computed tomography (CT) image and are employed as the input to k-Wave. To produce more realistic RF data, the following factors are added in sequential order to examine their individual impact on imaging: sound absorption, sensor frequency response, Gaussian noise, sensor location error, and mode conversion. A series of simulations are needed to fully compute $\frac{dG}{dt}$ in order to establish the MM. In simulations, a single transducer element is assigned as a source with an initial pressure being 1 Pa, whereas every image pixel in the ROI is a receiver. The received RF data at each receiver location is $\frac{dG}{dt}$ for the specific source and receiver locations. This simulation is repeated for all transducer elements and the FFT is applied to $\frac{dG}{dt}$ to obtain the frequency domain MM as indicated by Fig. 1.

### 2.5. Performance evaluation metrics

The accuracy of the FDMB method is assessed by the peak-signal-to-noise-ratio (PSNR) and the structural similarity (SSIM) to quantify the

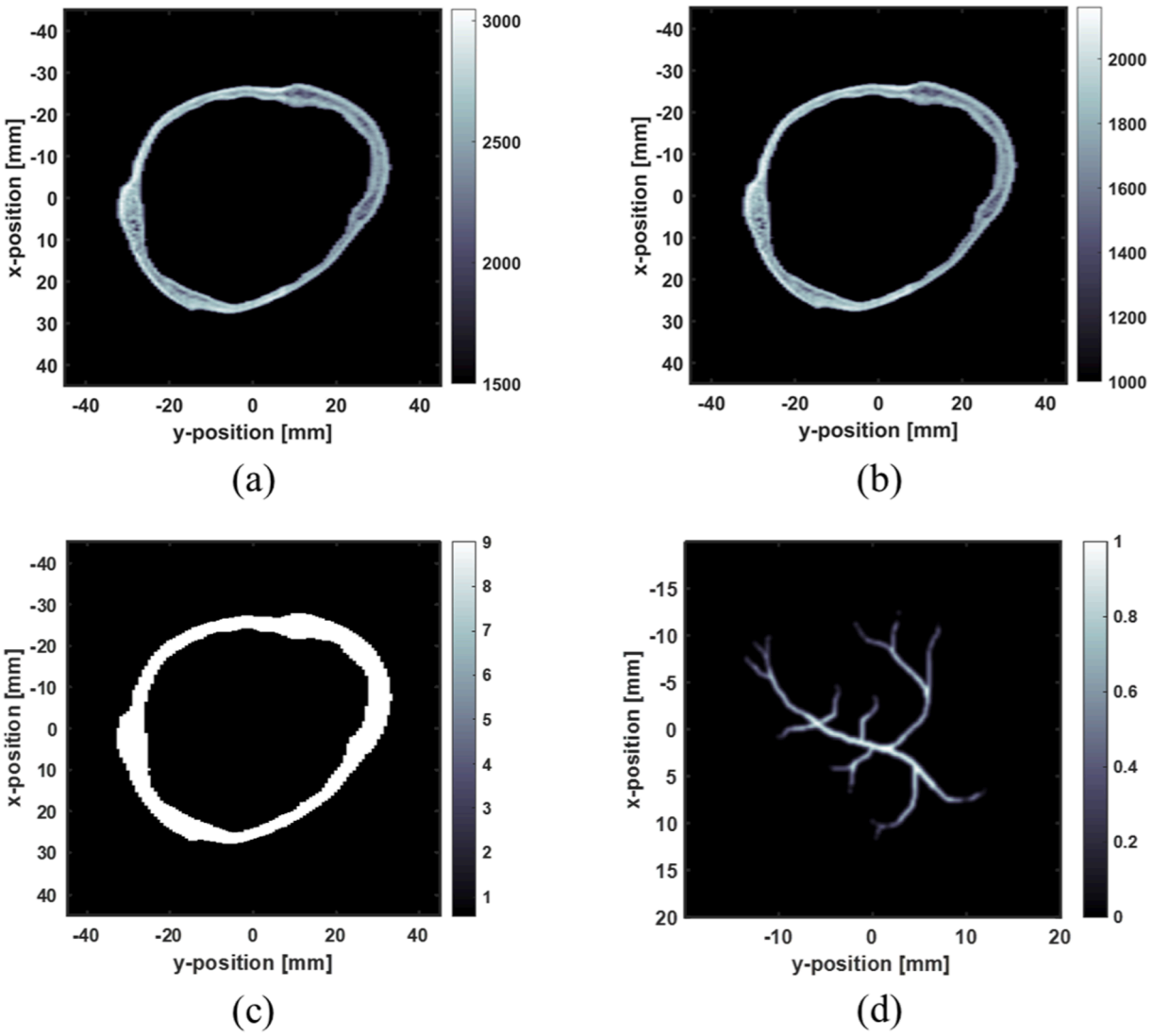


**Fig. 3.** (a) Speed of sound map, (b) density map, and (c) longitudinal wave absorption coefficient map of a rhesus monkey skull. (d) Blood vessel used in the numerical simulation.

quality of the reconstructed images.

#### 2.5.1. *Peak-signal-to-noise-ratio (PSNR)*

PSNR can be defined as a function of mean square error (MSE):

$$\mathrm{PSNR} = 20\log_{10}\left(\frac{p_{\max}}{\sqrt{\mathrm{MSE}}}\right) \tag{13}$$

where $p_{\max}$ is the maximum pixel value of the image.

#### 2.5.2. *Structural similarity (SSIM)*

SSIM is an image quality index that consists of luminance, contrast, and structure comparison terms:

$$l(x,y) = \frac{2\mu_x\mu_y + C_1}{\mu_x^2 + \mu_y^2 + C_1} \tag{13}$$

$$c(x,y) = \frac{2\sigma_x\sigma_y + C_2}{\sigma_x^2 + \sigma_y^2 + C_2} \tag{14}$$

$$s(x,y) = \frac{\sigma_{xy} + C_3}{\sigma_x\sigma_y + C_3} \tag{15}$$

where $C_1 = (K_1L)^2, C_2 = (K_2L)^2$ and $C_3 = \frac{C_2}{2}$. $L$ is the dynamic range of the pixel and $L = 255$ is used for 8 bits/pixel gray scale images. $K_1 = 0.01$ and $K_2 = 0.03$ are used [43]. The general form of SSIM is defined as Eq. (17):

$$\mathrm{SSIM}(x,y) = \frac{(2\mu_x\mu_y + C_1)(2\sigma_x\sigma_y + C_2)}{(\mu_x^2 + \mu_y^2 + C_1)(\sigma_x^2 + \sigma_y^2 + C_2)} \tag{17}$$

Averaging the SSIM across the ROI results in a single index that can be used to evaluate the quality of the reconstructed images.

## 3. Numerical results

In this section, 2D numerical analysis is performed to quantitatively evaluate the accuracy and image reconstruction time of the FDMB method. All reconstructions are performed using a graphic processing unit (GPU). The computer workstation is equipped with an AMD Ryzen 9 5950 X, 128 GB of memory at 3200 MHz, and an NVIDIA GeForce RTX 3090 (24 GB VRAM). The truncation value for the TSVD is selected for each case based on the best image quality that can be obtained. The pseudo-inverse is performed by "pinv" in MATLAB 2022.

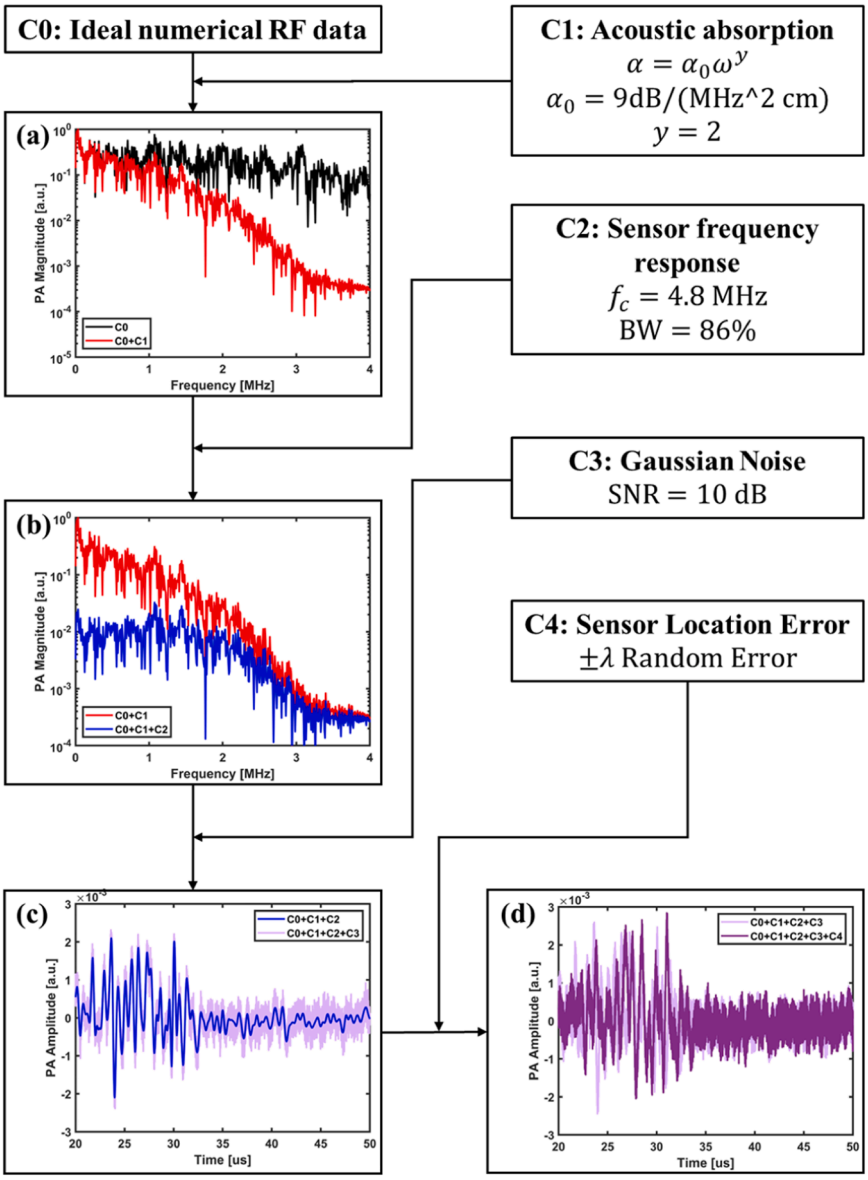


**Fig. 4.** Flowchart of numerical RF data calculation with realistic conditions for a transcranial photoacoustic tomography. Effect of (a) acoustic absorption, (b) sensor frequency response, (c) Gaussian noise, and (d) random sensor location error within one wavelength.

### 3.1. MB reconstruction in a homogeneous medium

The FDMB method is first analytically evaluated in a lossless homogeneous medium. The SOS is 1500 m/s and the density is 1000 kg/m$^3$. As a benchmark, the interpolated model matrix inversion (IMMI) method [25] is used for comparison. The IMMI method is also a model-based image reconstruction scheme but is performed in the time-domain. The optical absorption distribution of a truncated paraboloid source is used, and it can be described as:

$$H_x(x,y) = \begin{cases} 1 - \dfrac{x^2+y^2}{r_0^2}, x^2+y^2 < r_0^2 \\ 0, \&\text{otherwise} \end{cases} \tag{18}$$

where $r_0 = 1$ cm is the radius of the paraboloid source, which is illustrated in Fig. 2(a). Since $p_0 = \frac{\beta c^2}{C_p} = \Gamma H_x(x,y)$, the solution of Eq. (2) at the sensor location $r$ from the paraboloid center is [25]:

$$p(t) = \frac{\Gamma}{4\pi c}\frac{\partial}{\partial t}\left\{\phi(t)\left[1 - \frac{r^2+c^2t^2}{r_0^2}\right] + \frac{4ct}{r_0^2} r \sin\left[\frac{\phi(t)}{2}\right]\right\} \tag{19}$$

$$\phi(t) = \begin{cases} 2\cos^{-1}\left(\dfrac{r_0^2 - c^2t^2 - r^2}{2ctr^2}\right), \left|r_0^2 - c^2t^2 - r^2\right| < 2ctr^2 \\ 0, \&\text{otherwise} \end{cases} \tag{20}$$

PA signals from the given source are estimated at $r = 40$ mm and the number of transducer elements is 512 that are evenly distributed across 360°. To generate the synthetic RF data received by the sensors, a sampling frequency of 15 MHz is used, and the same sampling frequency is used when constructing the MM. The 2D analytical frequency-domain Green's function $G = \frac{i}{4}H_0^{(2)}(kr)$, where $H_n^{(2)}$ is the Hankel function of the second kind, is used for directly constructing the frequency-domain MM. For image reconstruction, the number of pixels is 200 for each axis and the pixel size is 0.2 mm. The truncation value $\sigma_k = 5.6 \times 10^{-41}$ is used for this study, which is the default value given by MATLAB. Down-sampling is not implemented while a threshold frequency of 2 MHz is used for truncation in the FDMB method.

Fig. 2(b) and (c) show the reconstructed images obtained by the IMMI and the FDMB methods, respectively. While the IMMI achieves almost exact reconstruction as shown in Fig. 2(d), the reconstructed

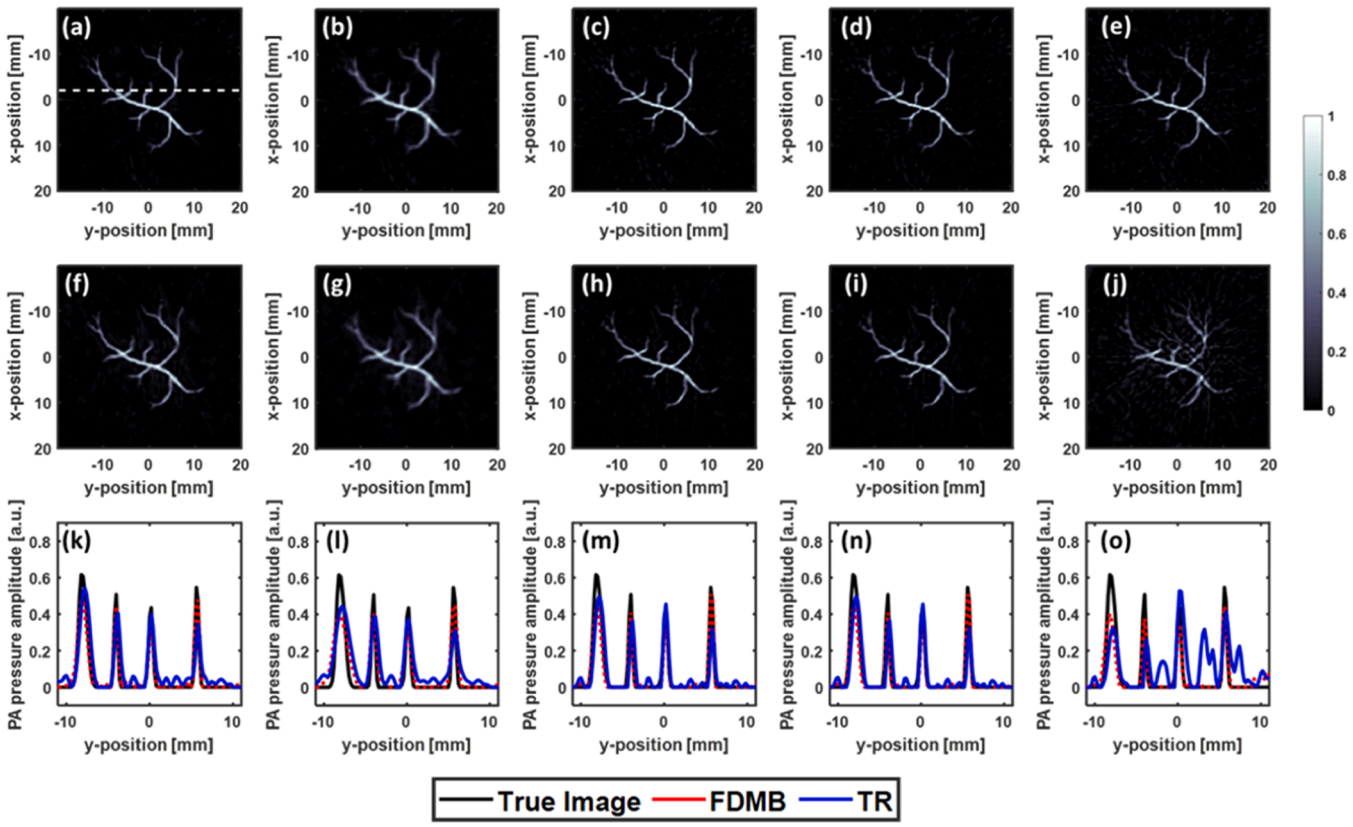


**Fig. 5.** Reconstructed images by the FDMB (first row) and the TR method (second row) with five different conditions. (a), (f) Considering only heterogeneities of SOS and density (C0). (b), (g) Adding acoustic absorption to the medium (C0 +C1). (c), (d) Adding sensor frequency response (C0 +C1 +C2) to PA signals. (d), (i) Adding 10 dB Gaussian noise to PA signals (C0 +C1 +C2 +C3). (e), (j) Considering $\pm\lambda$ random sensor location error for each sensor (C0 +C1 +C2 +C3 +C4). (k-o) Comparison of the true image, images obtained by the FDMB and TR methods along the line indicated as the white dashed line in (a).

image obtained by the FDMB method is shown to be less accurate than the IMMI method. Specifically, the FDMB method returns a slightly smaller paraboloid radius than the IMMI method does. It should also be noted that the FDMB method returns negative values around the edge of the paraboloid which are non-physical. The IMMI method, on the other hand, does not have this issue. Compared to the IMMI method, however, the FDMB method is considerably faster in computing the MM and reconstructing the image (>100 times and > 90 times faster, respectively). Furthermore, since frequency truncation can be performed by the FDMB method, the resulting MM size can also be considerably smaller than that of the IMMI method, leading to a less demand on the computational resource. It should be noted that this study does not conclude that the FDMB method is always faster than time-domain model-based methods, as IMMI is only one type of time-domain model-based method.

### 3.2. MB reconstruction in a heterogeneous medium

To validate the FDMB for transcranial PA imaging, numerical simulations are performed in a heterogeneous medium. For the MM and synthetic RF data calculation, full-wave simulations are conducted with the k-Wave MATLAB toolbox [42]. Medium properties including SOS and density shown in Fig. 3(a) and (b) are extracted from the CT scan image of a rhesus monkey skull and are used for both the MM and RF data calculation. Blood vessel shown in Fig. 3(d) is located inside the skull and used as the image target. The same sensor configuration used for the previous homogeneous medium is employed here to acquire synthetic RF data.

In addition to the medium heterogeneity, there are several other conditions that can be added to generate more realistic synthetic RF data as shown in Fig. 4. The first added condition (C1) is the acoustic absorption that follows a frequency power law [44]:

$$\alpha = \alpha_0 \omega^y \tag{21}$$

where $\alpha_0$ is the absorption coefficient in nepers $(\text{rad/s})^{-y}\,\text{m}^{-1}$, $\omega$ is the angular frequency, and $y$ is the power law exponent. When PA signals pass through the given skull, high frequency components decay more than low frequency components due to Eq. (21), therefore, the major components of PA signals detected by transducer elements are lower frequency components as shown in Fig. 4(a). The longitudinal wave absorption map is shown in Fig. 3(c). For a soft tissue illustrated as a black background, $\alpha_0 = 0.56\text{dB}/\text{MHz}^2\text{cm}$ and $y = 2$ is used [45]. Constant absorption is defined across the monkey skull where $\alpha_0 = 9\text{dB}/\text{MHz}^2\text{cm}$ and $y = 2$ are used [45]. While absorption is considered for synthetic RF data generation, it is not considered for image reconstruction. (i.e., not considered when computing the MM), for reasons that will be explained later.

The second condition considered (C2) is the sensor frequency response. Unlike backscattered ultrasound signals for B-mode ultrasound imaging, PA signals contain a broader frequency spectrum. Generally speaking, high frequency components are from the target boundary while low frequency components are from the center part of the target [46]. Considering a sensor frequency response acts as a bandpass filter which results in the loss of the low and high frequency components of PA signals as shown in Fig. 4(b). The center frequency of the filter $f_c$ is 4.8 MHz and the bandwidth (BW) is 86 % in accordance with an actual physical ring array in our lab, which we plan to use in the future experimental study.

The third condition (C3) is the effect of noise. There are two types of noise that can be considered for PAT. One is the thermal acoustic noise

**Table 1**
image quality index for the FDMB method and the TR method with five different conditions.

| | PSNR [dB] | | SSIM | |
|---|---|---|---|---|
| Conditions | FDMB | TR | FDMB | TR |
| C0 | 34.06 | 31.47 | 0.81 | 0.68 |
| C0 + C1 | 29.84 | 27.99 | 0.80 | 0.66 |
| C0 + C1 + C2 | 30.90 | 30.17 | 0.72 | 0.71 |
| C0 + C1 + C2 + C3 | 30.90 | 30.17 | 0.72 | 0.71 |
| C0 + C1 + C2 + C3 + C4 | 28.35 | 25.50 | 0.62 | 0.45 |

that has random distribution which can be modeled with Gaussian distribution [47]. The other noise comes from the ultrasound transducer that can be modeled as Johnson noise [48]. For simplicity, only thermal acoustic noise is considered, and 10 dB Gaussian noise is considered as shown in Fig. 4(c).

For the final condition, the effect of sensor location errors (C4) is studied. The exact sensor locations are not always known, and any errors in the sensor location naturally affect the accuracy of the MM, leading to distorted images. Random sensor location error $(e_x, e_y)$ is added to the original sensor element location. The total applied sensor location error $e = \sqrt{e_x^2 + e_y^2}$ is within one wavelength at the center frequency in water ($\lambda = 0.3125$mm). In this case, the RF data are obtained based on the sensor location displaced by $e$, while the MM is established based on the original sensor location.

A grid size of 0.04 mm and a CFL number of 0.2 are used to calculate both the synthetic RF data when considering only C0. The CFL number is reduced to 0.02 when computing the synthetic RF data whenever skull absorption is considered, because a large sound absorption requires a small time-step to achieve converged results in k-Wave. An acquisition time of 120 μs is selected for the synthetic RF data and the MM calculation. To compute an accurate MM, a small grid point is required to describe the relation between sensors and pixels. However, using the same small computational grid for imaging results in long image reconstruction time. To address this issue, different grid sizes are adopted to compute the MM and to perform image reconstruction. Specifically, the image pixel size is set at 0.2 mm, while a grid size of 0.067 mm (three times smaller than the image pixel size) is used for the MM calculation. Each simulation requires about 65 s and the total duration for the MM calculation is about 9.3 h. The MM consumes 8.6 GB of storage after down-sampling and frequency truncation. The computational grid for the MM calculation can accommodate frequency components up to 11.236 MHz. Since frequency truncation at 2 MHz is applied, the MM operates within the frequency range supported by the designated computational grid.

The TR method is also implemented here for comparison. A spatial resolution of 0.2 mm and a CFL of 0.2 are used to reconstruct images by the TR method. For all images, there are 200 pixels in each direction. The spatial resolutions used to compute the MM and TR are chosen to be different from the one used for simulating the RF data to avoid the inverse crime. Although attenuation can be compensated both in the TR [21] and FDMB methods, absorption is not considered during reconstruction, as noise will be also amplified due to the inverse of absorption and could result in image reconstruction failure.

Fig. 5. shows the images obtained by the FDMB and the TR methods. Here, the negative values which have no physical meaning are replaced with zero for both the FDMB and the TR methods. The corresponding image quality indices are shown in Table 1. The images on the first row of Fig. 5 are obtained by the FDMB method while the images on the second row are from the TR method. The third row shows the comparison of cross-sectional profiles of the true image and images obtained by the FDMB and the TR methods along the white dashed line indicated in Fig. 5(a). Each column indicates different conditions shown in Fig. 4. For the first four columns and the last column, $\sigma_k$ of 10 and 13 are selected, respectively, for the TSVD.

The first column corresponds to C0 which is the baseline and only considers medium heterogeneities. For this baseline condition, the image obtained by the FDMB method reconstructs pressure amplitudes that are better matched with the ones from the true image, while yielding a background noise level lower than that of the TR method as shown in Fig. 5(k). The second column shows the reconstructed images adding the acoustic absorption (C0 +C1). Compared to the first column, both the FDMB and TR methods result in a more blurred boundary of the blood vessel, due to the fact that the skull acts like a low-pass filter, removing the high-frequency components that are related to the edge. The FDMB image, though, still shows a slightly better sharpness than the TR image, as suggested by Fig. 5(l). The third column corresponds to C0 +C1 +C2 where the sensor frequency response is added. This condition is equivalent to applying a band pass filter and the remaining low frequency components are significantly reduced as shown in Fig. 4(b). Compared to the previous results, both the FDMB and the TR method return narrower blood vessels. This is attributed to the loss of low frequency components which enhance the sharpness. Furthermore, replacement of negative values to zero along the blood vessel edges also contributes to narrowing the width of the blood vessels. The fourth column presents the images with 10 dB Gaussian noise (C0 +C1 +C2 +C3). It is observed that both the FDMB and the TR methods are robust against this level of noise. The results are almost identical with or without the noise, as seen by comparing Fig. 5(m) and (n). The last column shows the effect of sensor location errors. As shown in Fig. 5(e) and (f), the sensor location error considered in this study seems to have the largest effect among all, leading to strong image artifacts particularly for the TR method.

Overall, the FDMB shows similar image quality to that of the TR methods. Furthermore, the reconstruction time using the FDMB method

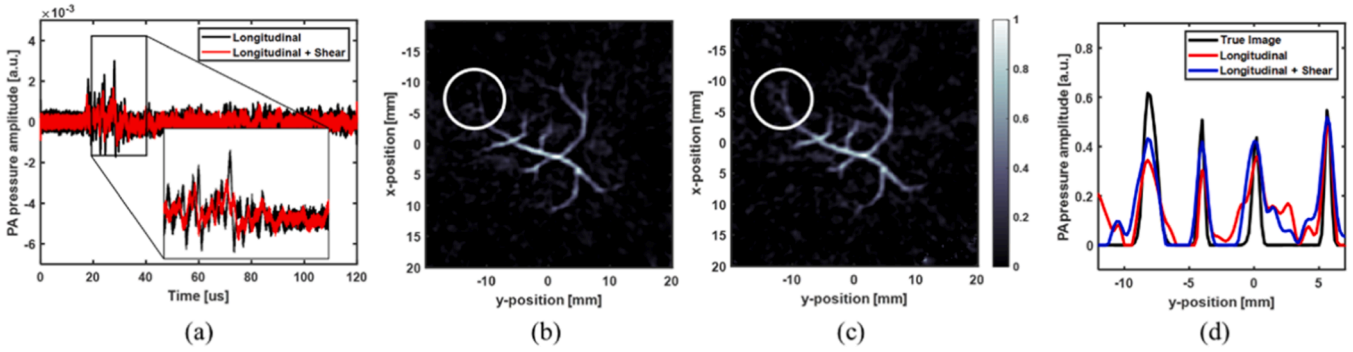


**Fig. 6.** (a) Comparison of RF data considering only longitudinal and shear waves. Image reconstruction using RF data considering mode conversion and the MM (b) without considering mode conversion, the MM (c) considering mode conversion. (d) Comparison of the cross-sectional profiles of true image, images obtained by the FDMB with the MM with and without mode conversion. Cross sectional line is indicated as the white dashed line in Fig. 5. (a).

is approximately 0.3 s (including FFT of the RF data, data truncation, and down-sampling), while TR method requires 5.37 s, which is 17.9 times slower. This indicates that the FDMB method can generate images significantly faster than the TR method and has the potential for real-time imaging.

### 3.3. Shear wave consideration

In theory, transmission of PA signals through the skull could also experience mode conversion. Depending on the angle of incidence, when the incident longitudinal waves encounter the boundary of the soft tissue and skull, the transmitted waves split into both longitudinal and shear waves. In this section, a single layer skull (same shape of skull as used above but with homogeneous acoustical properties) is considered because k-Wave simulations fail to provide converged elastic wave results when using the full heterogeneous skull model. However, the result presented in this section can still shed light on the effect of mode conversion in the FDMB method. The skull is assumed to have shear wave absorption of $\alpha_S = 20\text{dB/MHz}^2\text{cm}$, while the longitudinal wave absorption is $\alpha_L = 9\text{dB/MHz}^2\text{cm}$ [45]. The shear wave SOS of the skull is assumed to be 1550 m/s and the longitudinal wave SOS of the skull is assumed to be 3047 m/s. An example of PA signal is shown in Fig. 6(a), comparing the cases with and without the mode conversion. In addition to mode conversion, absorption, sensor frequency response, Gaussian noise, and sensor location error (C0 +C1 +C2 +C3 +C4) have also been considered in generating synthetic PA signals. Both the MM without mode conversion and the MM with mode conversion are considered to obtain images and assess the merit of incorporating mode conversion. $\sigma_k$ of 17 and 24 are selected for the MM without mode conversion and with mode conversion, respectively. Fig. 6(b) and (c) show the obtained images without mode conversion and with mode conversion for the MM calculation, respectively. It is observed that incorporating mode conversion for the MM can better capture more details, such as small vessel branches highlighted with a white circle in Fig. 6(c). However, the image obtained by the MM without mode conversion shows slightly better noise level, and therefore, image quality indices for both conditions are similar. PSNR values for the MM without mode conversion and the MM with mode conversion are both 25 dB while SSIM values are 0.49 and 0.48, respectively.

The computation time of the MM with mode conversion is 8.5 times longer than that of the MM without mode conversion, when using k-Wave for both simulations. Nevertheless, the image reconstruction time is the same with and without considering mode conversion.

## 4. Discussion and conclusion

This study presents a FDMB method to achieve rapid image reconstruction for transcranial photoacoustic imaging. This approach is based on the photoacoustic forward model which is a linear function of the initial pressure distribution and can be described by a MM. Prior to imaging, the frequency-domain MM is analytically or numerically calculated. The solution (initial pressure distribution) to the linear system in the frequency-domain can be obtained by Moore-Penrose pseudo-inverse. Since the MM is independent of the image objects as it only depends on the medium and the geometry between the transducer and imaging pixels, it can be established and inverted prior to imaging for repeated use. Regularization methods such as TSVD can be used to solve ill-posed problems and result in improved image quality. To improve image reconstruction speed, down-sampling is used, and the high-frequency components of the MM and RF data are truncated. Due to the high absorption of the skull, high frequency components are naturally filtered out and therefore have minimal impact on image reconstruction.

To evaluate the performance and verify the FDMB method, the image reconstruction is first performed in a homogeneous medium. The IMMI method is used as a benchmark. While the FDMB method is less accurate than the IMMI method in that it produces negative values around the target boundary, it achieves significantly faster MM calculation and image reconstruction times ($>$ 100 times and $>$ 90 times, respectively) compared to the IMMI method due to the smaller matrix size resulted from down-sampling and frequency truncation. There are several methods available to mitigate negative values that can arise from both time-domain and frequency-domain model-based methods [49,50]. However, these non-negative constraints methods are iterative in nature, tend to be slow, and are not suited for real-time imaging. Therefore, our future work aims to develop a more robust method to eliminate these non-physical negative values without replacing negative values to zero as a solution.

The numerical analysis is then performed to quantitatively evaluate the image reconstruction with a rhesus monkey skull under five different conditions: medium heterogeneities, acoustic absorption, sensor frequency response, Gaussian noise, and sensor location errors. The TR method is selected as a benchmark for comparison. For the baseline condition (C0), the FDMB method returns higher pressure magnitudes and better contrast than the TR method and yields better PSNR (34.06 dB vs 31.47 dB) and SSIM (0.81 vs 0.68) values.

When the acoustic absorption is applied (C0 +C1), skull layer performs like a low-pass filter, which removes the high frequency components. Since high frequency components are related to the target boundary, both the FDMB and the TR methods return more blurry images than the previous condition as shown in Fig. 5(l), resulting in lower image quality indices. The FDMB method, however, still yields a better PSNR (29.84 dB vs 27.99 dB) and SSIM (0.80 vs 0.66).

The effect of sensor frequency response is then studied. This can be understood as the band-pass filtering, which removes remaining low and high frequency components. However, because the skull absorption has already removed the high frequency components, the effect of the band-pass filtering is mainly on the low-frequency part. Both images obtained by the FDMB and TR methods show narrower blood vessels compared to the previous condition as shown in Fig. 5(m). This result can be attributed to the combined effect of the removal of low frequency components and alteration of negative values to zero along the blood vessel edges. Furthermore, the reconstructed pressure magnitudes in both the FDMB and TR methods are higher than the previous condition, resulting in improved contrast in the obtained images. For the FDMB method, the PSNR value increases by 1.06 dB while the SSIM value decreases by 0.08 compared to the previous condition. For the TR method, both the PSNR and the SSIM values increase by 2.18 dB and 0.05, respectively.

The Gaussian noise of 10 dB (C3) is further added to assess the robustness of the developed algorithm against noise. It is observed that both the FDMB and TR methods are insensitive to this level of noise and show identical PSNR and SSIM compared to the previous condition. For the FDMB method, this robustness against noise might arise from the combined effect of the image reconstruction process as described by Eq. (12), which bears resemblance to averaging and the TSVD. Specifically, the FDMB method reconstructs image by multiplying the model matrix $\boldsymbol{M}(\omega_i)$ and $\boldsymbol{P}(\omega_i)$ for each frequency, subsequently averaging the resultant matrix post-summation. This averaging could potentially mitigate random noise interference, enhancing image quality. Furthermore, the incorporation of the TSVD, a commonly used technique for noise removal, further enhances robustness against noise [51,52]. On the other hand, TR inherently integrates over the entire domain for every location, which could also be interpreted as a form of averaging, thus reducing the noise.

The sensor location error is employed as a final condition (C4). It is observed that this condition results in the lowest PSNR and SSIM values for both the FDMB and TR methods. The obtained image by the FDMB method, however, shows less artifacts and better PSNR (28.35 dB vs 25.50 dB) and SSIM (0.62 vs 0.45) values than the TR method. It should be noted that, for the TR method, the image quality can be improved by employing interpolation of the RF data. For example, when we increase

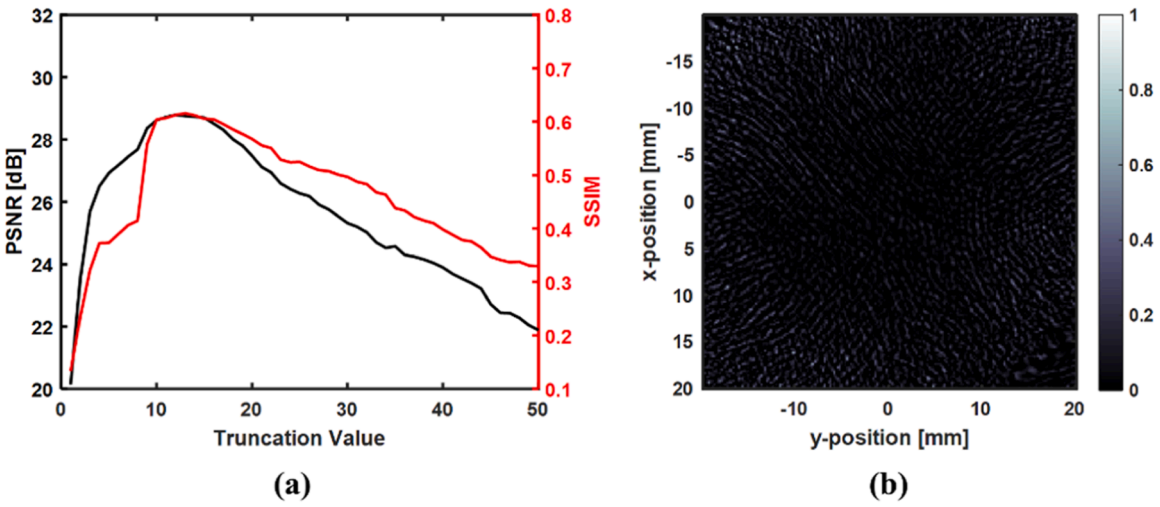


**Fig. 7.** (a) PSNR and SSIM values for the condition (C0-C4) with varying truncation values. (b) The obtained image without regularization.

the number of sensor elements from 512 to 1132 using interpolation based on the nearest neighbor algorithm, better sharpness and noise levels can be achieved, resulting in slightly higher PSNR (28.35 dB vs 29.41 dB) and SSIM (0.62 vs 0.68) values than the FDMB method can achieve.

The merit of incorporating mode conversion for the MM is also assessed. For this study, the single-layer skull model is employed due to failure of obtaining converged elastic wave results with the full heterogeneous skull model by k-Wave MATLAB toolbox. It is observed that incorporating mode conversion for the MM returns in better details. However, it also introduces a slightly higher background noise level compared to the MM without mode conversion, resulting in similar image quality indices. The high absorption of shear waves can be identified as one possible reason for their limited impact. However, since the single-layer skull model is used, further studies are needed with the fully heterogeneous skull model. One disadvantage of incorporating shear waves is that it becomes significantly more computationally expensive for building the MM, though this increase in computation does not affect the actual image reconstruction time.

Overall, the resulting images show that the FDMB method returns similar image quality compared to the TR method. However, it achieves 17.9 times faster image reconstruction time than the TR method because the FDMB method involves a simple matrix multiplication. Fast image reconstruction using the FDMB method is further enabled by removing high frequency components ($>$ 2 MHz) and down-sampling.

Although the FDMB method offers significant advantages in image reconstruction speed in heterogeneous media with comparable image quality compared to the traditional TR method, there are still some limitations that need to be addressed. Like other MB methods, the MM can be very large. Although down-sampling and frequency truncation can partially address these issues, the FDMB method still requires significant computational resources, especially when extended to 3D imaging. However, it is still feasible to achieve the equivalent reconstruction time for 3D imaging by keeping the size of the MM while employing a larger spatial resolution. For example, the MM storage size used for this study is 8.6 GB. With the voxel size of 1 mm, the 3D ROI would be 40mm $\times$ 40mm $\times$ 25mm to maintain the MM size. Therefore, by compromising the spatial resolution, we can still achieve near-real time 3D imaging. Another limitation of the FDMB method is that the exact acoustic property map is required for the MM calculation. This study assumes that the acoustic property map is known. In practice, the skull's profile and acoustic properties can be obtained by CT scans [16]. There are also ongoing efforts to extract skull properties and profiles using ultrasound [53–55]. Sensitivity to the regularization scheme is also a challenge of the FDMB method. Fig. 7(a) shows the PSNR and SSIM values with different truncation values for the condition (C0-C4). Fig. 7(b) also shows the image without regularization, to emphasize the importance of regularization. While regularization can significantly improve the image quality obtained by the FDMB method, it is important to note that the choice of the truncation values has a non-trivial effect on the image quality. In each case, the truncation value for the TSVD should be carefully selected to maximize the image quality.

Moreover, the current two-dimensional (2D) model cannot account for the out-of-plane reflection and refraction. To conduct more accurate simulations, 3D numerical models have to be used in the future. Finally, the current MM calculation assumes point-like transducers. This assumption is often not satisfied in the experimental setting and can induce errors. To address this issue, the transducer spatial impulse response (SIR) can be readily integrated into the MM [56,57], which would be crucial for the future experimental validation of the FDMB method.

## Funding source

NIH R21EB027981 and NIH R01EB031629.

## Declaration of Competing Interest

There are no competing interests to declare.

## Data availability

Data will be made available on request.

## Acknowledgements

We would like to thank Dr. Amir Rosenthal for the helpful discussion and providing the IMMI MATLAB code. This work was partially supported by the United States National Institutes of Health (NIH) grants R21EB027981 and R01EB031629.

## Appendix

This appendix presents the derivation of Eq. (2). When considering instantaneous heating (satisfying stress confinement), the photoacoustic process can be reformulated as an initial value problem where there is no explicit source term [34], and Eq. (1) can be rewritten as:

$$\rho(\mathbf{x})\nabla\cdot\left(\frac{1}{\rho(\mathbf{x})}\nabla p(\mathbf{x},t)\right)-\frac{1}{c^2(\mathbf{x})}\frac{\partial^2 p(\mathbf{x},t)}{\partial t^2}=0 \tag{21}$$

with initial conditions

$$p|_{t=0}=p_0(\mathbf{x}),\left.\frac{\partial p}{\partial t}\right|_{t=0}=0 \tag{22}$$

The first initial condition defines the initial acoustic pressure due to instantaneous heating. The second initial condition assumes that the initial particle velocity is zero [58]. Eq. (21) can be solved with the Green's function $G$, which is defined as:

$$\rho(\mathbf{x})\nabla\cdot\left(\frac{1}{\rho(\mathbf{x})}\nabla G(\mathbf{x},t;\mathbf{x}',t')\right)-\frac{1}{c^2(\mathbf{x})}\frac{\partial^2 G(\mathbf{x},t;\mathbf{x}',t')}{\partial t^2}=-\delta(\mathbf{x}-\mathbf{x}')\delta(t-t') \tag{23}$$

By multiplying $G$ to Eq. (21) and multiplying $p(\mathbf{x},t)$ to Eq. (22), and subtracting them, we obtain:

$$p(\mathbf{x},t)\delta(\mathbf{x}-\mathbf{x}')\delta(t-t')=\rho(\mathbf{x})\left[G\nabla\cdot\left(\frac{1}{\rho(\mathbf{x})}\nabla p(\mathbf{x},t)\right)-p(\mathbf{x},t)\nabla\cdot\left(\frac{1}{\rho(\mathbf{x})}\nabla G\right)\right]+\frac{1}{c^2(\mathbf{x})}\left[p(\mathbf{x},t)\frac{\partial^2 G}{\partial t^2}-G\frac{\partial^2 p(\mathbf{x},t)}{\partial t^2}\right] \tag{24}$$

By integrating over $\mathbf{x}$ in the volume of interest $V$ and over $t$ from 0 to $t^+$, Eq. (24) becomes:

$$p(\mathbf{x}',t')=\int_0^{t^+}dt\int_V d\mathbf{x}\quad\rho(\mathbf{x})\left[G\nabla\cdot\left(\frac{1}{\rho(\mathbf{x})}\nabla p(\mathbf{x},t)\right)-p(\mathbf{x},t)\nabla\cdot\left(\frac{1}{\rho(\mathbf{x})}\nabla G\right)\right]+\int_0^{t^+}dt\int_V d\mathbf{x}\quad\frac{1}{c^2(\mathbf{x})}\left[p(\mathbf{x},t)\frac{\partial^2 G}{\partial t^2}-G\frac{\partial^2 p(\mathbf{x},t)}{\partial t^2}\right] \tag{25}$$

In the absence of acoustic boundary conditions, the first integral vanishes, and Eq. (25) can be simplified to:

$$p(\mathbf{x}',t')=\int_V d\mathbf{x}\quad\frac{1}{c^2(\mathbf{x})}\left[p(\mathbf{x},t)\frac{\partial G}{\partial t}-G\frac{\partial p(\mathbf{x},t)}{\partial t}\right]\Bigg|_{t=0} \tag{26}$$

With initial conditions presented in Eq. (22), Eq. (26) can be written as:

$$p(\mathbf{x}',t')=\int_V\frac{p_0(\mathbf{x})}{c^2(\mathbf{x})}\frac{\partial G}{\partial t}d\mathbf{x} \tag{27}$$

Finally, Eq. (27) can be rewritten as Eq. (2) by interchanging the variables $\mathbf{x}$ and $\mathbf{x}'$, as well as $t$ and $t'$.

## References


[1] L. Luo, E.M. Callaway, K. Svoboda, Genetic dissection of neural circuits, Neuron 57 (2008) 634–660.

[2] B.B. Biswal, M. Mennes, X.-N. Zuo, S. Gohel, C. Kelly, S.M. Smith, C.F. Beckmann, J.S. Adelstein, R.L. Buckner, S. Colcombe, A.-M. Dogonowski, M. Ernst, D. Fair, M. Hampson, M.J. Hoptman, J.S. Hyde, V.J. Kiviniemi, R. Kötter, S.-J. Li, C.-P. Lin, M.J. Lowe, C. Mackay, D.J. Madden, K.H. Madsen, D.S. Margulies, H.S. Mayberg, K. McMahon, C.S. Monk, S.H. Mostofsky, B.J. Nagel, J.J. Pekar, S.J. Peltier, S. E. Petersen, V. Riedl, S.A.R.B. Rombouts, B. Rypma, B.L. Schlaggar, S. Schmidt, R. D. Seidler, G.J. Siegle, C. Sorg, G.-J. Teng, J. Veijola, A. Villringer, M. Walter, L. Wang, X.-C. Weng, S. Whitfield-Gabrieli, P. Williamson, C. Windischberger, Y.-F. Zang, H.-Y. Zhang, F.X. Castellanos, M.P. Milham, Toward discovery science of human brain function, Proc. Natl. Acad. Sci. USA 107 (2010) 4734–4739.

[3] L.J. Hogstrom, S.M. Guo, K. Murugadoss, M. Bathe, Advancing multiscale structural mapping of the brain through fluorescence imaging and analysis across length scales, Interface Focus 6 (2016), 20150081.

[4] E.M.C. Hillman, Optical brain imaging in vivo: techniques and applications from animal to man, J. Biomed. Opt. 12 (2007), 051402.

[5] F. Helmchen, W. Denk, Deep tissue two-photon microscopy, Nat. Methods 2 (2005) 932–940.

[6] S. Ogawa, T.M. Lee, A.R. Kay, D.W. Tank, Brain magnetic resonance imaging with contrast dependent on blood oxygenation, Proc. Nat. Acad. Sci. USA 87 (1990) 9868–9872.

[7] G.H. Glover, Overview of functional magnetic resonance imaging, Neurosurg. Clin. N. Am. 22 (2011) 133–139.

[8] S. Hu, L.V. Wang, Neurovascular photoacoustic tomography, Front. Neuroenergetics 2 (2010) 10.

[9] L.V. Wang, S. Hu, Photoacoustic tomography: in vivo imaging from organelles to organs, Science 335 (2012) 1458–1462.

[10] E. Brown, J. Brunker, S.E. Bohndiek, Photoacoustic imaging as a tool to probe the tumour microenvironment, Dis. Model Mech. 12 (2019), dmm039636.

[11] L.V. Wang, J. Yao, A practical guide to photoacoustic tomography in the life sciences, Nat. Methods 13 (2016) 627–638.

[12] X. Wang, Y. Pang, G. Ku, X. Xie, G. Stoica, L.V. Wang, Noninvasive laser-induced photoacoustic tomography for structural and functional in vivo imaging of the brain, Nat. Biotechnol. 21 (2003) 803–806.

[13] Z. Xu, Q. Zhu, L.V. Wang, In vivo photoacoustic tomography of mouse cerebral edema induced by cold injury, J. Biomed. Opt. 16 (2011), 066020.

[14] X. Wang, D.L. Chamberland, G. Xi, Noninvasive reflection mode photoacoustic imaging through infant skull toward imaging of neonatal brains, J. Neurosci. Methods 168 (2008) 412–421.

[15] X. Wang, J.B. Fowlkes, D.L. Chamberland, G. Xi, P.L. Carson, Reflection mode photoacoustic imaging through infant skull toward noninvasive imaging of neonatal brains, in: in: Photons Plus Ultrasound: Imaging and Sensing 2009, 7177, SPIE, 2009, pp. 74–81.

[16] C. Huang, L. Nie, R.W. Schoonover, Z. Guo, C.O. Schirra, M.A. Anastasio, L. V. Wang, Aberration correction for transcranial photoacoustic tomography of primates employing adjunct image data, J. Biomed. Opt. 17 (2012), 066016.

[17] L. Nie, X. Cai, K. Maslov, A. Garcia-Uribe, M.A. Anastasio, L.V. Wang, Photoacoustic tomography through a whole adult human skull with a photon recycler, J. Biomed. Opt. 17 (2012), 110506.

[18] B. Liang, S. Wang, F. Shen, Q.H. Liu, Y. Gong, J. Yao, Acoustic impact of the human skull on transcranial photoacoustic imaging, Biomed. Opt. Express 12 (2021) 1512–1528.

[19] E. Bossy, K. Daoudi, C. Boccara, M. Tanter, J.-F. Aubry, G. Montaldo, M. Fink, Time reversal of photoacoustic waves, Appl. Phys. Lett. 89 (2006), 184108, 184108–184108.

[20] R. Kowar, Time reversal for photoacoustic tomography based on the wave equation of Nachman, Smith, and Waag, Phys. Rev. E Stat. Nonlinear Soft Matter Phys. 89 (2014), 023203.

[21] B.E. Treeby, E.Z. Zhang, B.T. Cox, Photoacoustic tomography in absorbing acoustic media using time reversal, Inverse Probl. 26 (2010), 115003.

[22] L. Ding, X.L. Dean-Ben, D. Razansky, Real-time model-based inversion in cross-sectional optoacoustic tomography, IEEE Trans. Med. Imaging 35 (2016) 1883–1891.

[23] A. Pattyn, Z. Mumm, N. Alijabbari, N. Duric, M.A. Anastasio, M. Mehrmohammadi, Model-based optical and acoustical compensation for photoacoustic tomography of heterogeneous mediums, Photoacoustics 23 (2021), 100275.

[24] J. Prakash, H. Dehghani, B.W. Pogue, P.K. Yalavarthy, Model-resolution-based basis pursuit deconvolution improves diffuse optical tomographic imaging, IEEE Trans. Med. Imaging 33 (2014) 891–901.

[25] A. Rosenthal, D. Razansky, V. Ntziachristos, Fast semi-analytical model-based acoustic inversion for quantitative optoacoustic tomography, IEEE Trans. Med. Imaging 29 (2010) 1275–1285.

[26] A. Rosenthal, V. Ntziachristos, D. Razansky, Model-based optoacoustic inversion with arbitrary-shape detectors, Med. Phys. 38 (2011) 4285–4295.
[27] X.L. Deán-Ben, D. Razansky, A practical guide for model-based reconstruction in optoacoustic imaging, Front. Phys. 10 (2022).
[28] V. Perrot, M. Polichetti, F. Varray, D. Garcia, So you think you can DAS? A viewpoint on delay-and-sum beamforming, Ultrasonics 111 (2021), 106309.
[29] M. Xu, L.V. Wang, Universal back-projection algorithm for photoacoustic computed tomography, Phys. Rev. E Stat. Nonlinear Soft Matter Phys. 71 (2005), 016706.
[30] D. Queirós, X.L. Déan-Ben, A. Buehler, D. Razansky, A. Rosenthal, V. Ntziachristos, Modeling the shape of cylindrically focused transducers in three-dimensional optoacoustic tomography, J. Biomed. Opt. 18 (2013), 076014.
[31] J. Jose, R.G.H. Willemink, W. Steenbergen, C.H. Slump, T.G. van Leeuwen, S. Manohar, Speed-of-sound compensated photoacoustic tomography for accurate imaging, Med. Phys. 39 (2012) 7262–7271.
[32] C. Zhang, Y. Wang, A reconstruction algorithm for thermoacoustic tomography with compensation for acoustic speed heterogeneity, Phys. Med Biol. 53 (2008) 4971–4982.
[33] J. Poudel, S. Na, L.V. Wang, M.A. Anastasio, Iterative image reconstruction in transcranial photoacoustic tomography based on the elastic wave equation, Phys. Med. Biol. 65 (2020), 055009.
[34] B.T. Cox, S. Kara, S.R. Arridge, P.C. Beard, k-space propagation models for acoustically heterogeneous media: application to biomedical photoacoustics, J. Acoust. Soc. Am. 121 (2007) 3453–3464.
[35] Y. Zhou, J. Yao, L.V. Wang, Tutorial on photoacoustic tomography, JBO 21 (2016), 061007.
[36] C.B. Shaw, J. Prakash, M. Pramanik, P.K. Yalavarthy, Least squares QR-based decomposition provides an efficient way of computing optimal regularization parameter in photoacoustic tomograpy, J. Biomed. Opt. 18 (2013) 80501.
[37] R. Penrose, A generalized inverse for matrices, Math. Proc. Camb. Philos. Soc. 51 (1955) 406–413.
[38] C. Fenu, L. Reichel, G. Rodriguez, H. Sadok, GCV for Tikhonov regularization by partial SVD, Bit Numer. Math. 57 (2017) 1019–1039.
[39] M. Fuhry, L. Reichel, A new Tikhonov regularization method, Numer. Algorithm 59 (2012) 433–445.
[40] P.C. Hansen, Analysis of discrete Ill-posed problems by means of the L-curve, SIAM Rev. 34 (1992) 561–580.
[41] V.V. Selivanov, M.D. Lepage, R. Lecomte, Real-time PET image reconstruction based on regularized pseudo-inverse of the system matrix, in: Proceedings of the IEEE Nuclear Science Symposium Conference Record (Cat. No.01CH37310) (2001), 3, 1737–1741.
[42] B.E. Treeby, B.T. Cox, k-Wave: MATLAB toolbox for the simulation and reconstruction of photoacoustic wave fields, J. Biomed. Opt. 15 (2010), 021314.
[43] Z. Wang, E.P. Simoncelli, A.C. Bovik, Multiscale structural similarity for image quality assessment, in: Proceedings of the Thrity-Seventh Asilomar Conference on Signals, Systems & Computers, 2003 (2003), 2, 398–1402.
[44] Diagnostic Ultrasound Imaging: Inside Out, first ed., ⟨https://shop.elsevier.com/books/diagnostic-ultrasound-imaging-inside-out/szabo/978-0-12-680145-3⟩.
[45] B.E. Treeby, T. Saratoon, The contribution of shear wave absorption to ultrasound heating in bones: Coupled elastic and thermal modeling, in: Proceedings of the IEEE International Ultrasonics Symposium (IUS) (2015), 1–4.
[46] W. Choi, D. Oh, C. Kim, Practical photoacoustic tomography: realistic limitations and technical solutions, J. Appl. Phys. 127 (2020), 230903.
[47] E.R. Hill, W. Xia, M.J. Clarkson, A.E. Desjardins, Identification and removal of laser-induced noise in photoacoustic imaging using singular value decomposition, Biomed. Opt. Express 8 (2016) 68–77.
[48] A.M. Winkler, K. Maslov, L.V. Wang, Noise-equivalent sensitivity of photoacoustics, J. Biomed. Opt. 18 (2013), 097003.
[49] L. Ding, X.L. Deán-Ben, C. Lutzweiler, D. Razansky, V. Ntziachristos, Efficient non-negative constrained model-based inversion in optoacoustic tomography, Phys. Med. Biol. 60 (2015) 6733.
[50] Image rEconstruction in Cross-sectional Optoacoustic Tomography Based on Non-negative Constrained Model-based inversion. ⟨https://opg.optica.org/abstract.cfm?uri=ecbo-2015-953919⟩.
[51] R. Francischello, M. Geppi, A. Flori, E.M. Vasini, S. Sykora, L. Menichetti, Application of low-rank approximation using truncated singular value decomposition for noise reduction in hyperpolarized 13C NMR spectroscopy, NMR Biomed. 34 (2021), e4285.
[52] S.K. Jha, R.D.S. Yadava, Denoising by singular value decomposition and its application to electronic nose data processing, IEEE Sens. J. 11 (2011) 35–44.
[53] L. Guasch, O. Calderón Agudo, M.-X. Tang, P. Nachev, M. Warner, Full-waveform inversion imaging of the human brain, NPJ Digit Med 3 (2020), 28.
[54] T. Wang, Y. Jing, Transcranial ultrasound imaging with speed of sound-based phase correction: a numerical study, Phys. Med. Biol. 58 (2013) 6663.
[55] M. Hajian, R. Gaspar, R.G. Maev, Accurate 3-D profile extraction of skull bone using an ultrasound matrix array, IEEE Trans. Biomed. Eng. 64 (2017) 2858–2871.
[56] C. Huang, K. Wang, L. Nie, L.V. Wang, M.A. Anastasio, Full-wave iterative image reconstruction in photoacoustic tomography with acoustically inhomogeneous media, IEEE Trans. Med. Imaging 32 (2013) 1097–1110.
[57] K.B. Chowdhury, M. Bader, C. Dehner, D. Jüstel, V. Ntziachristos, Individual transducer impulse response characterization method to improve image quality of array-based handheld optoacoustic tomography, Opt. Lett. 46 (2021) 1–4.
[58] Fast calculation of pulsed photoacoustic fields in fluids using k-space methods, The Journal of the Acoustical Society of America, AIP Publishing. ⟨https://pubs.aip.org/asa/jasa/article-abstract/117/6/3616/543464/Fast-calculation-of-pulsed-photoacoustic-fields-in?redirectedFrom=fulltext⟩.

**Hyungjoo Park** received the B.Eng. degree in automotive engineering from Kookmin University, Seoul, South Korea, in 2017 and the M.S. degree in mechanical engineering from University of Cincinnati, Cincinnati, OH, USA, in 2020. He is currently pursuing the Ph.D. degree in acoustics at the Pennsylvania State University, University Park, PA, USA. His research focuses on image reconstruction algorithms for fast transcranial photoacoustic imaging.

**Junjie Yao** is currently an Associate Professor at the Department of Biomedical Engineering at Duke University. Dr. Yao received his B.S. (2006) and M.S. (2008) degrees in Biomedical Engineering from Tsinghua University (Beijing, China), and his Ph.D. degree in Biomedical Engineering at Washington University in St. Louis in 2013. More information about Dr. Yao's research at http://photoacoustics.pratt.duke.edu/

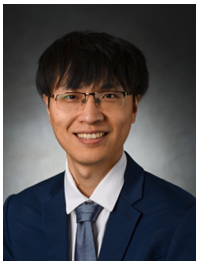

**Yun Jing** is currently a Professor of the Graduate Program in Acoustics at the Pennsylvania State University. Dr. Jing received his B.S. (2006) degree in Acoustics from Nanjing University (Nanjing, China), and his Ph.D. degree in Architectural Acoustics from Rensselaer Polytechnic Institute in 2009. More information about Dr. Jing's research at https://sites.psu.edu/jinglab/.